RESEARCH MEMORANDUM

for the

Air Materiel Command, U. S. Air Force

LOW-LIFT DRAG AND DUCT PRESSURE RECOVERY OF A $\frac{1}{8.25}$-SCALE MODEL OF THE CONSOLIDATED VULTEE XF-92 AIRPLANE AT MACH NUMBERS FROM 0.7 TO 1.4

By Grady L. Mitcham, Joseph E. Stevens, Norman L. Crabill, and Arthur H. Hinners, Jr.

Langley Aeronautical Laboratory
Langley Field, Va.

NATIONAL ADVISORY COMMITTEE FOR AERONAUTICS

WASHINGTON

NACA RM SL51E23

NATIONAL ADVISORY COMMITTEE FOR AERONAUTICS

RESEARCH MEMORANDUM

for the

Air Materiel Command, U. S. Air Force

LOW-LIFT DRAG AND DUCT PRESSURE RECOVERY OF A $\frac{1}{8.25}$ - SCALE MODEL OF THE CONSOLIDATED VULTEE XF-92 AIRPLANE AT MACH NUMBERS FROM 0.7 TO 1.4

By Grady L. Mitcham, Joseph E. Stevens, Norman L. Crabill, and Arthur H. Hinners, Jr.

SUMMARY

A flight investigation has been made to determine the external drag and pressure recovery of a $\frac{1}{8.25}$ - scale flight model of the Consolidated Vultee XF-92 from Mach numbers 0.7 to 1.4 and Reynolds numbers from 8.5×10^6 to 19.2×10^6 at or near zero lift.

Relative mass flow, average pressure recovery, total drag, internal drag, and external drag are presented as functions of Mach number.

Between Mach numbers of 0.90 and 0.975, the external drag of the configuration (including base drag of the inner body and additive drag) was about equal to that of a similar model with a faired nose and no mass flow; however, at supersonic speeds the drag coefficient for the faired-nose model remained relatively constant whereas the drag coefficient for the ducted model continued to increase sharply. The internal drag coefficient of the duct was roughly constant at 0.013 up to a Mach number of 1.20, after which it decreased to 0.0075 at a Mach number of 1.4. The over-all pressure recovery of the inlet and duct varied from 94 percent at a Mach number of 0.7 to about 91 percent at a Mach number of 1.4 at a relative-mass-flow ratio of about 0.30. The losses in pressure recovery were believed to be caused by the possible occurrence of separation of flow from the inner body and by an aerodynamically unclean internal configuration which did not duplicate the form proposed for the original XF-92 airplane.

INTRODUCTION

At the request of the Air Materiel Command, U. S. Air Force, flight tests of modified $\frac{1}{8.25}$ - scale rocket-powered models of the Consolidated Vultee XF-92 airplane have been executed to evaluate the drag and longitudinal stability and control characteristics at transonic and low-supersonic speeds. The models tested previously were modifications of the XF-92 in that the nose was a faired body of revolution which completely closed the duct. Results from three of these tests have been presented in reference 1.

An unmodified model with an external-compression nose inlet of the type and form proposed for the XF-92 airplane was then tested at the request of the contractor. The present investigation is only of secondary interest as regards to the over-all XF-92 rocket-model program, its primary purpose being to present information on the original-inlet configuration. Although this inlet was apparently designed for high-supersonic speeds, this test was made to determine its transonic and low-supersonic external drag and pressure recovery because of the interest in its performance under off-design conditions.

A choking constriction was used to produce a quantity of air flow which would approximate that of a turbojet or ram-jet-powered model wherein the back pressure is produced with a flame front and burner. In the proposed XF-92, the inner body ends at a point just behind the wing trailing edge; in the model tested, it was extended to the exit to provide instrumentation space. Since the internal configuration of this model was not aerodynamically clean and did not duplicate that of the proposed airplane, the determination of pressure recovery was of secondary interest.

The investigation was conducted by the Pilotless Aircraft Research Division (at its testing station at Wallops Island, Va.).

Ground tests were conducted in the preflight jet described in reference 2 at Mach numbers of 0.71 and 1.4 to select the locations of a limited number of survey tubes to be used in the flight test to determine mass flow and pressure recovery. The results of the subsonic test were expected to be applicable over a fairly large Mach number range since the duct Mach number was expected to be approximately a constant.

The flight-test data were obtained during unpowered coasting flight as the model decelerated through the Mach number range between 1.4 and 0.7 at approximately zero lift. The relative-mass-flow ratio was nearly constant at 0.30.

[redacted]

SYMBOLS

A	duct cross-sectional area, square feet
a_l/g	longitudinal accelerometer reading, positive forward along the longitudinal axis
a_n/g	normal accelerometer reading, positive toward the top of the model
$\bar{c}$	wing mean aerodynamic chord, feet
C_D	coefficient of drag $\left(\text{Drag}/q_f S\right)$
C_{L_α}	rate of change of lift coefficient with angle of attack, per degree
H	total-pressure-tube reading, pounds per square foot
M	Mach number
m	mass flow, slugs per second
m_0	mass of air flowing through a stream tube of area (0.390 sq ft) equal to the inlet-cowl area under free-stream conditions
P	static pressure, pounds per square foot
q	dynamic pressure, pounds per square foot
R	gas constant, 1715 foot-pounds per slug-degree Rankine
r	radial distance from center line of model, feet
S	total wing area of model (including portion within fuselage), 6.25 square feet
T	temperature, degrees Rankine
V	velocity, feet per second
W	weight of model, 160.1 pounds
α	angle of attack, degrees

[redacted]

γ	specific-heat ratio (value taken as 1.40)
θ_c	angle between inlet axis and surface of cone, degrees (see fig. 3)
θ_l	cowling-position parameter, angle between axis of inlet and straight line that connects vertex of cone with lip of cowling, degrees (see fig. 3)
μ	viscosity of air, slugs per foot per second
ρ	mass density of air, slugs per cubic foot
φ	angular location of survey tubes in duct, measured from vertical center line of model, degrees (fig. 8)

Subscripts:

av	average
c	cowl entrance
ex	exit
ext	external
f	free stream
FT	flight test
GT	ground test
i	inner
int	internal
L	local
o	outer
s	stagnation
T	total
47	station 47, the plane of survey

[redacted]

MODEL AND APPARATUS

Model.- A three-view drawing of the model used in the present investigation is shown in figure 1. The physical characteristics and weight and balance data are presented in table I. Figure 1 indicates the contour of the inner body, and the section views on the same figure show the division of the annular duct by islands supporting the inner body. The islands consisted of the wing and fin roots and a simulated nose-wheel-well fairing in the lower duct. A cutaway drawing of the model is shown in figure 2.

The external-compression nose inlet had a cone angle θ_c of 25° and a cowling-lip angle θ_l of 32°. A conical shock from the point of the cone would intersect the cowling lip at a free-stream Mach number of 3.8. Coordinates and a cross-sectional view of the inlet are given in figure 3. A plot of the duct cross-sectional area from the cowling lip to the exit is shown in figure 4. The ratio of annular-inlet area to maximum fuselage cross-sectional area is 0.317. The structural islands supporting the inner body, instrumentation hatch covers, sheet-metal joints, and protruding bolt and rivet heads inside the duct produced an aerodynamically unclean internal configuration. The choking constriction (fig. 1) at station 50 was constructed of 35 machine screws, equally spaced around the annular duct, and fitted with sleeves to produce the desired choking area. Photographs of the model are shown as figures 5 and 6. The control surfaces that appear in figure 5 were held fixed at 0° deflection throughout the flight.

The model was boosted to $M = 1.45$ by a solid-fuel, 6-inch-diameter Deacon rocket motor which produces an average thrust of 6500 pounds for approximately 3.1 seconds.

Launching was accomplished from a zero-length launcher as shown in figure 7. The booster was attached to the model with a piston and cylinder unit containing a small powder charge. At cessation of booster thrust, the charge was ignited and the expanding gases forced the model and booster to separate.

Ground-test apparatus.- Ground tests were made in the preflight free jet, described in reference 2, at Wallops Island, Va. The tests were made with a 27-inch subsonic nozzle and a 12-inch nozzle designed to produce a Mach number of 1.4. In these tests, free-stream stagnation temperature was obtained by thermocouples and was recorded by an oscillograph. Air heaters permitted control of temperature during the tests and the air was dried prior to the test.

[redacted]

Within the model, 23 total-pressure tubes and 7 static-pressure orifices were utilized to survey one-half the duct. Figure 8 shows a cross section of the duct at station 47 and indicates the locations at which total- and static-pressure measurements were taken. Three additional static orifices ($\varphi = 0^\circ$, 90°, and 180°) were located at station 57.83 (fig. 9) near the duct exit. All duct pressures and free-stream total pressure were measured by optical-recording six-cell manometers.

A photograph of the model mounted before the Mach number 1.4 nozzle in the preflight jet is shown as figure 10.

Flight-test apparatus.- The telemetered flight data consisted of 8 pressure measurements at station 47 (5 total pressures and 3 static pressures), 3 static-pressure measurements at the duct exit, total pressure measured on the total-pressure tube under the model (fig. 1), normal acceleration, and longitudinal acceleration for a total of 14 channels of information. Ground equipment consisting of the Doppler radar and the radar tracking unit was used to determine free-stream velocity and position in space. Free-stream temperature and static pressure were obtained from a radiosonde released immediately after the model flight.

GROUND TESTS

Radial total-pressure-recovery profiles obtained from the ground tests at $M = 0.71$ are given in figure 11 for the rakes located at $\varphi = 0^\circ$, 45°, 90°, and 135°. The local total-pressure recoveries were determined as the ratio of measured total pressure to free-stream total pressure. The radial total-pressure-recovery profiles were integrated to give the average radial-pressure recovery at that radius. The variation of this average radial-total-pressure recovery with φ at $M = 0.71$ is shown in figure 12.

The test for $M = 1.4$ was made in a 12-inch free jet. The entrance of the model proved to be too large for this jet at the mass-flow ratio of the test, and the resulting oblique shock - jet-boundary interaction produced flow conditions at the model entrance which did not duplicate the free-stream conditions. This test did show, however, that, in spite of the increased disturbances of the flow at the model entrance, the general shape of the mass flow and pressure-recovery profiles were not different from the subsonic-test profiles. It was assumed, therefore, that the results of the test at $M = 0.71$ were adequate to select the flight-test pressure tubes and to calculate flight-test mass flow and pressure recovery.

[redacted]

The flight-test tubes, indicated in figures 8 and 12, were selected to give a representative total pressure which would require only a small correction factor to give the average total pressure as explained in the section, "BASIS OF ANALYSIS."

BASIS OF ANALYSIS

Ground tests.- Mass flow was computed from the equation

$$m_{47} = 2\sqrt{\frac{\gamma}{RT_s}}\int_0^{\pi}\int_{r_i}^{r_o} P_L M_L \sqrt{1 + 0.2M_L^2}\; r\, dr\, d\varphi$$

where M_L is found from the local values of static pressure and total pressure.

The inner integral was determined for each of the rakes containing four total-pressure tubes located at $\varphi = 0^\circ$, 45°, 90°, and 135°. Then by assuming appropriate profiles, this integral was determined for the single total-pressure tubes located at $\varphi = 4.8^\circ$, 9.6°, 75.5°, 82.8°, 158.8°, 169.6°, and 180°. The flow was assumed to be symmetrical in both ducts, and the total mass flow was assumed to be twice the mass flow obtained from the integration.

Relative mass flow was computed from

$$\frac{m_{47}}{m_0} = \frac{m_{47}}{\rho_f V_f A_c}$$

where $A_c = \frac{\pi}{4}(\text{diameter cowl})^2$

The average Mach number of the complete duct was determined by solving the equation

$$\left(M_{47}\sqrt{1 + 0.2M_{47}^2}\right)_{av} = \frac{m_{47}\sqrt{T_s}}{\sqrt{\frac{\gamma}{R}}\, A_{47} P_{47_{av}}}$$

[redacted]

for M_{47}, the average Mach number at station 47. Then, pressure recovery

$$\frac{\left(H_{47}\right)_{av}}{H_f} = \frac{P_{47}}{\left(\frac{P}{H}\right)_{47}} \frac{1}{H_f}$$

where $\left(\frac{P}{H}\right)_{47}$ is obtained from tables as functions of M_{47}.

The average total pressure at the survey station, as obtained from the tubes subsequently used in the flight test, was computed from

$$\left(H_{47}\right)_{av} = H_{47_{av_{FT}}} \text{ (Correction factor)}$$

where the correction factor was determined at $M = 0.71$ from the ground tests and was assumed to be a constant with M.

Flight test.- The free-stream Mach number was determined from: (a) The velocity as recorded by the CW Doppler radar set and the free-stream temperature taken from the radiosonde measurements (b) The total pressure H measured on the total-pressure tube underneath the model (fig. 1) and the free-stream static pressure P as measured by the radiosonde

For $M_f < 1$

$$\frac{H}{P} = \left(1 + \frac{\gamma}{\gamma - 1} M_f^2\right)^{\frac{\gamma}{\gamma-1}} \tag{1}$$

For $M_f > 1$

$$\frac{H}{P} = \frac{\left(\frac{\gamma + 1}{2} M_f^2\right)^{\frac{\gamma}{\gamma-1}}}{\left(\frac{2\gamma}{\gamma + 1} M_f^2 - \frac{\gamma - 1}{\gamma + 1}\right)^{\frac{1}{\gamma-1}}} \tag{2}$$

method (b) was used from $M = 1.05$ to 0.70 where changes in the basic pitching moment (reference 1) caused flight-path changes which the Doppler radar unit could not follow accurately. At $M = 1.05$, the total pressure computed from the CW Doppler radar set agreed with the measured value.

The flight-test mass flow was assumed to be proportional to the average of $\int_{r_i}^{r_o} \rho Vr \, dr$ computed for the five total-pressure tubes used in the flight test. At each of these total-pressure tubes selected,

$$\left(\int_{r_i}^{r_o} \rho Vr \, dr\right)_{FT} = \sqrt{\frac{\gamma}{R}}\left(P_L M_L \frac{\sqrt{1 + 0.2M_L^2}}{\sqrt{T_s}}\right)_{FT}\left(\frac{\int \rho Vr \, dr}{\rho Vr}\right)_{GT} r \qquad (3)$$

where $\left(\int \rho Vr \, dr\right)_{GT}$ represents the ground-test value for the rake containing the tube selected and $(\rho Vr)_{GT}$ is the ground-test value for the tube selected. Then

$$m_{FT} = \frac{\left(\int \rho Vr \, dr\right)_{FT_{av}}}{\left(\int \rho Vr \, dr\right)_{GT_{av}}} m_{GT} \qquad (4)$$

where the numerator is the average of the $\int \rho Vr \, dr$ for all flight-test total-pressure tubes and the denominator is the average of the corresponding tubes in the ground test.

Relative mass flow and pressure recovery were calculated as in the ground test.

The internal drag, the summation of the viscous and gage pressure forces acting in the duct minus the additive drag, was calculated from

$$C_{D_{int}} = \frac{1}{q_f S}\left[m_{47}\left(V_f - V_{ex}\right) - \left(P_{ex} - P_f\right)A_{ex}\right] \qquad (5)$$

The three exit static pressures were averaged to obtain the value of P_{ex} for use in equation (5).

The exit Mach number was ascertained from the equation

$$M_{ex}\sqrt{1 + \frac{\gamma - 1}{2}M_{ex}^2} = \frac{P_{47}A_{47}M_{47}\sqrt{1 + \frac{\gamma - 1}{2}M_{47}^2}}{P_{ex}A_{ex}} \qquad (6)$$

[redacted]

The exit velocity was then determined from this Mach number by calculating the exit temperature and speed of sound.

The total drag of the model was calculated from

$$C_{D_T} = \frac{W/S}{q_f}\left(\frac{a_n}{g}\sin\alpha - \frac{a_l}{g}\cos\alpha\right) \tag{7}$$

Since the model carried no angle-of-attack indicator, α was determined from

$$\alpha = \frac{a_n}{g}\frac{W/S}{q_f}\frac{1}{C_{L_\alpha}} \tag{8}$$

The accelerations a_n/g and a_l/g were obtained from the telemeter trace. Values for C_{L_α} were obtained from the tests on the modified XF-92 models mentioned previously (see reference 1). The computed angle of attack varied from 0.8° to -0.4°.

The external drag, the component in the drag direction of the viscous and pressure forces acting on the external surfaces of the body (including inner-body base drag), plus the additive drag, was determined from

$$C_{D_{ext}} = C_{D_T} - C_{D_{int}} \tag{9}$$

PRECISION OF DATA

The maximum value of the errors of the more important data is estimated as follows:

C_{D_T} at supersonic speeds	±0.001
C_{D_T} at subsonic speeds	±0.003
H_{47}/H_f	±0.04
m_{47}/m_0	±0.03
Mach number	±0.02

RESULTS AND DISCUSSION

Reynolds number.- The Reynolds number $\rho V\bar{c}/\mu$ of the flight test is given as a function of Mach number in figure 13.

Relative-mass flow.- The variation of relative mass flow with Mach number is shown in figure 14. No unsteady flow conditions were detected in either the ground or flight tests.

Total-pressure recovery.- The total-pressure recovery at station 47 as obtained from the flight test is presented in figure 15. The pressure recovery decreased from 94 percent at $M = 0.7$ to approximately 91 percent at $M = 1.4$. The Mach number at station 47 was 0.44.

The total-pressure losses associated with this type of diffuser should be of small value in this Mach number range. For example, reference 3 reports a test of a similar-type inlet at $M = 1.33$ with $\theta_c = 25^\circ$, $\theta_l = 36^\circ$, and a relative-mass-flow ratio of 0.5, in which a pressure recovery of 95 percent was obtained. An aerodynamically clean diffuser, however, was utilized in the referenced test.

In this test, with a relative-mass-flow ratio of 0.3, separation of the flow from the central body in the vicinity of the inlet possibly occurred and resulted in total-pressure losses. This effect did not show up noticeably in the shape of total-pressure-recovery profiles because of the survey-rake distance from the point of separation and mixing of the flow between these points. Figure 4, the variation of duct cross-sectional area, shows how the internal-flow area changed irregularly through the duct because of the wing and fin islands and the simulated-nose-wheel-well fairings. These area irregularities, the large amounts of wetted area, and the previously mentioned bolt and rivet heads, sheet metal joints, and so forth also contributed significantly to the total-pressure losses.

Drag.- The total drag coefficient of the configuration, presented in figure 16, is seen to be large at all Mach numbers. The internal drag coefficient was roughly constant at 0.013 in the transonic region and decreased to 0.0075 at $M = 1.4$. The external drag coefficient, which includes base drag over the base of the inner body, 0.196 square foot, and the additive drag, is compared with the drag coefficient (including base drag over the same fraction of the entire base area) obtained from unpublished tests on the faired-nose XF-92 model mentioned in the introduction. The drag rise of both models occurs at about $M = 0.9$. Between $M = 0.9$ and $M = 0.975$ the drag coefficients

[redacted]

for the two models were about the same when the accuracy of the subsonic drag is considered; however, the drag coefficient for the faired-nose model reaches a value of 0.034 at $M = 1.1$ and remains relatively constant to $M = 1.4$ whereas the drag coefficient for the ducted model continues to increase throughout the supersonic-speed range covered by the test.

CONCLUSIONS

1. The external drag coefficient of the configuration (including inner-body base drag and additive drag) was about equal to the total drag coefficient of a similar model with a faired nose between Mach numbers of 0.90 and 0.975; however, the drag coefficient of the ducted model continued to increase sharply at supersonic speeds whereas the drag coefficient for the faired-nose model remained relatively constant.

2. The over-all total-pressure recovery of the inlet and duct varied from approximately 94 percent at $M = 0.7$ to 91 percent at $M = 1.4$ at a relative-mass-flow ratio of about 0.30. The low pressure recovery

[redacted]

was believed to be caused by the aerodynamically unclean internal configuration and by the possible flow separation from the central body.

Langley Aeronautical Laboratory
National Advisory Committee for Aeronautics
Langley Field, Va.

Grady L. Mitcham

Grady L. Mitcham
Aeronautical Engineer

Joseph E. Stevens by GLM

Joseph E. Stevens
Aeronautical Research Scientist

Norman L. Crabill

Norman L. Crabill
Aeronautical Research Scientist

Arthur H. Hinners Jr.

Arthur H. Hinners, Jr.
Aeronautical Research Scientist

Approved:

Robert R. Gilruth
Chief of Pilotless Aircraft Research Division

JBB

[redacted]

REFERENCES

1. Mitcham, Grady L., Stevens, Joseph E., and Norris, Harry P.: Aerodynamic Characteristics and Flying Qualities of a Tailless Triangular-Wing Airplane Configuration as Obtained from Flights of Rocket-Propelled Models at Transonic and Low Supersonic Speeds. NACA RM L9L07, 1950.

2. Faget, Maxime A., Watson, Raymond S., and Bartlett, Walter A., Jr.: Free-Jet Tests of a 6.5-Inch-Diameter Ram-Jet Engine at Mach Numbers of 1.81 and 2.00. NACA RM L50L06, 1951.

3. Ferri, Antonio, and Nucci, Louis M.: Preliminary Investigation of a New Type of Supersonic Inlet. NACA TN 2286, 1951.

[redacted]

TABLE I

PHYSICAL CHARACTERISTICS AND WEIGHT AND BALANCE DATA OF

A $\frac{1}{8.25}$ - SCALE MODEL OF THE XF-92 AIRPLANE

Wing:	
Area (included), sq ft	6.25
Span, ft	3.80
Aspect ratio	2.31
Mean aerodynamic chord, ft	2.19
Sweepback of leading edge, deg	60
Dihedral (relative to mean thickness line), deg	0
Taper ratio (Tip chord/Root chord)	0
Airfoil section	NACA $65_{(06)}$A006.5
Vertical tail:	
Area (outside of fuselage), sq ft	0.81
Height (outside of fuselage), ft	0.97
Aspect ratio	2.31
Sweepback of leading edge, deg	60
Taper ratio (Tip chord/Root chord)	0
Airfoil section	NACA $65_{(06)}$A006.5
Weight and balance:	
Weight, lb	160.1
Wing loading, lb/sq ft	25.6
Center-of-gravity position, percent M.A.C.	23.7
Moment of inertia in pitch, slug ft^2	9.17

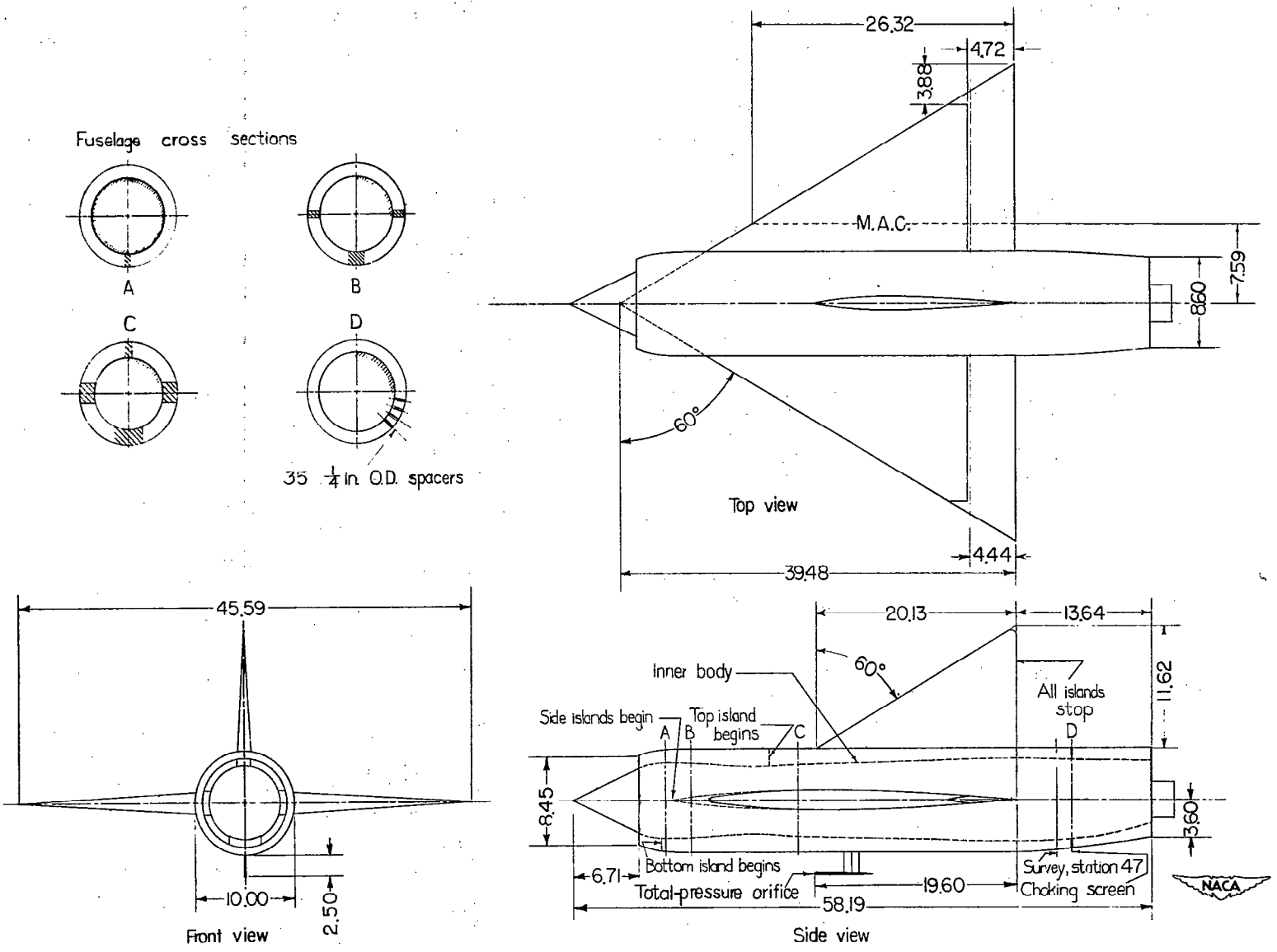

Figure 1.- Three-view drawing of the rocket-powered model. All dimensions are in inches.

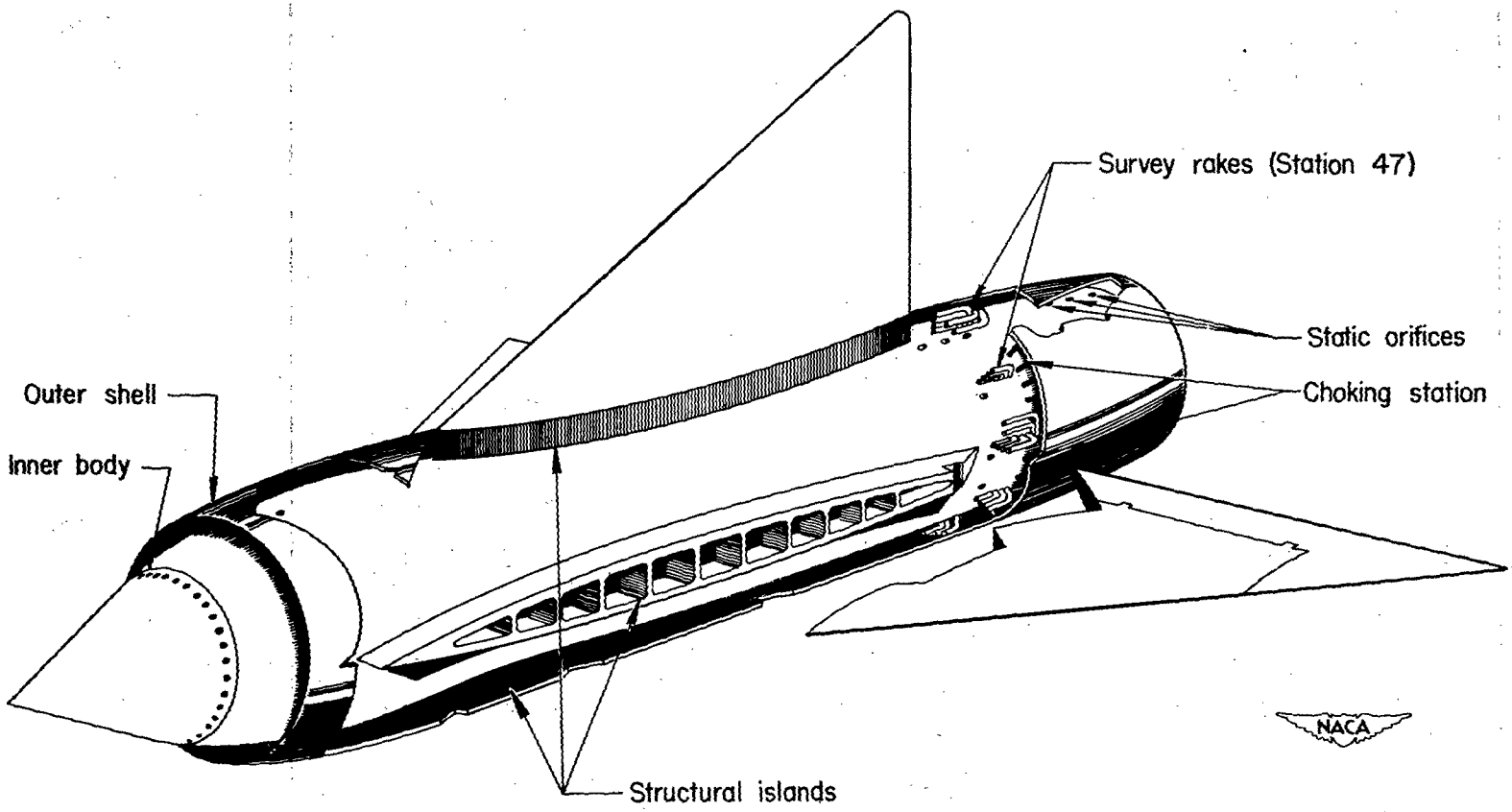

Figure 2.- Cutaway view of the model showing the internal arrangement.

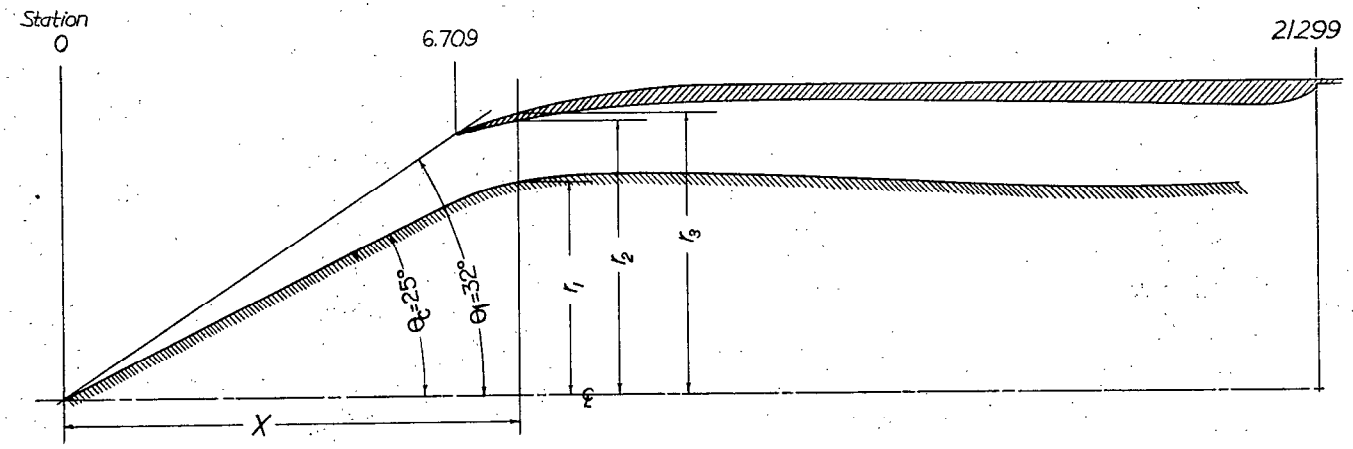

Inlet co-ordinates, in inches

Inner-body radius

X	r_1
0	0
6.513	3.031
6.709	3.118
6.815	3.162
7.128	3.272
7.440	3.359
7.753	3.426
8.065	3.475
8.378	3.509
8.690	3.534
9.003	3.553
9.315	3.565
9.628	3.575
9.840	3.579
10.253	3.579
10.565	3.577
10.878	3.569
11.190	3.562
11.503	3.552
11.815	3.542
12.128	3.530
12.440	3.518
12.753	3.508
13.065	3.491
13.378	3.474
13.690	3.453
14.003	3.444
14.315	3.429
14.628	3.410
14.940	3.394
15.253	3.376
15.565	3.358
15.878	3.340
16.190	3.323
16.815	3.304
17.440	3.300
18.065	3.306
18.690	3.318
19.315	3.335
19.940	3.351
20.565	3.368

Outer-body radii

X	r_2	r_3
6.709	4.203	4.242
6.815	4.237	4.282
7.128	4.323	4.391
7.440	4.395	4.488
7.753	4.453	4.573
8.065	4.504	4.648
8.378	4.549	4.714
8.690	4.587	4.772
9.003	4.620	4.823
9.315	4.648	4.865
9.628	4.672	4.901
9.940	4.692	4.930
10.253	4.706	4.954
10.565	4.717	4.972
10.878	4.724	4.986
11.190	4.728	4.995
11.503	4.730	4.999
11.815	4.729	5.000
12.128	4.729	↑
12.440	4.729	↓
12.753	4.728	↓
13.065	4.727	5.000
13.378	4.725	5.000
13.690	4.724	↑
14.003	4.723	↓
14.315	4.722	↓
14.628	4.718	↓
14.940	4.715	↓
15.253	4.711	↓
15.565	4.708	↓
15.878	4.703	↓
16.109	4.699	↓
16.503	4.695	↓
16.815	4.690	↓
17.128	4.686	↓
17.440	4.681	↓
17.753	4.675	↓
18.065	4.671	↓
18.378	4.665	↓
18.690	4.659	↓
19.003	4.652	↓
19.315	4.646	↓
19.628	4.641	↓
19.940	4.636	5.000

Figure 3.- Inlet configuration and coordinates. All dimensions are in inches.

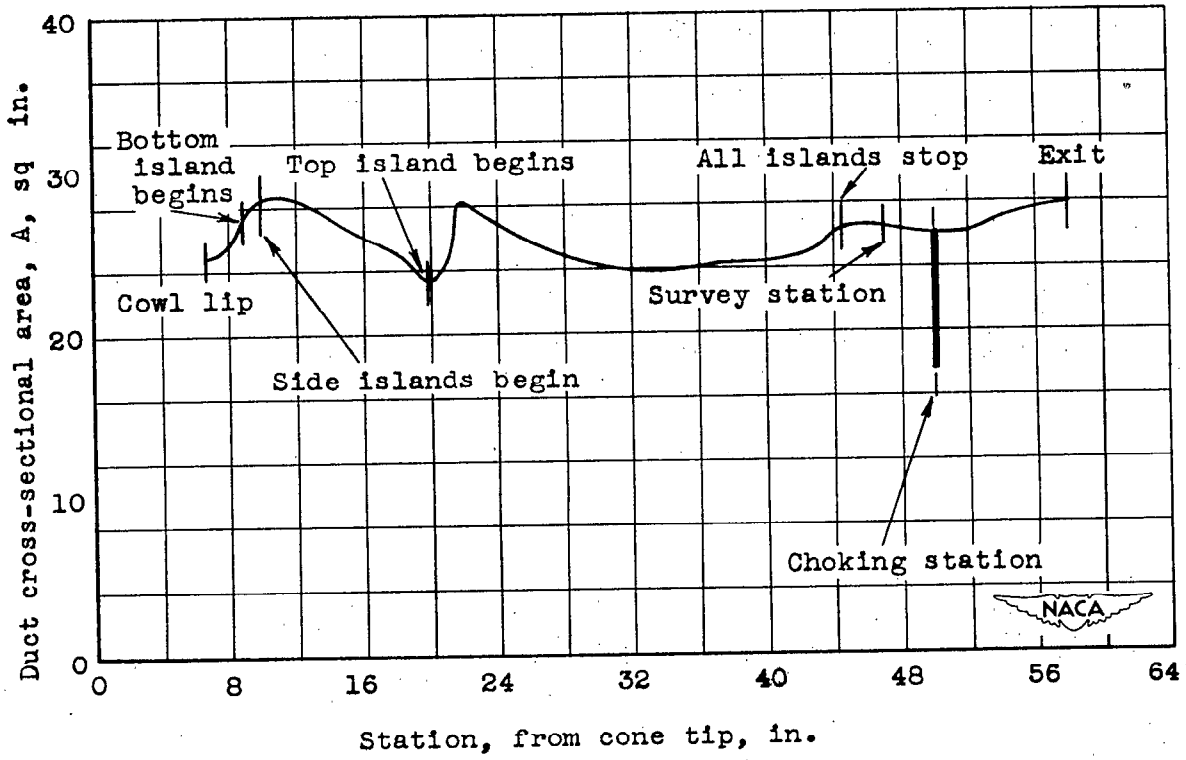

Figure 4.- Variation of duct cross-sectional area.

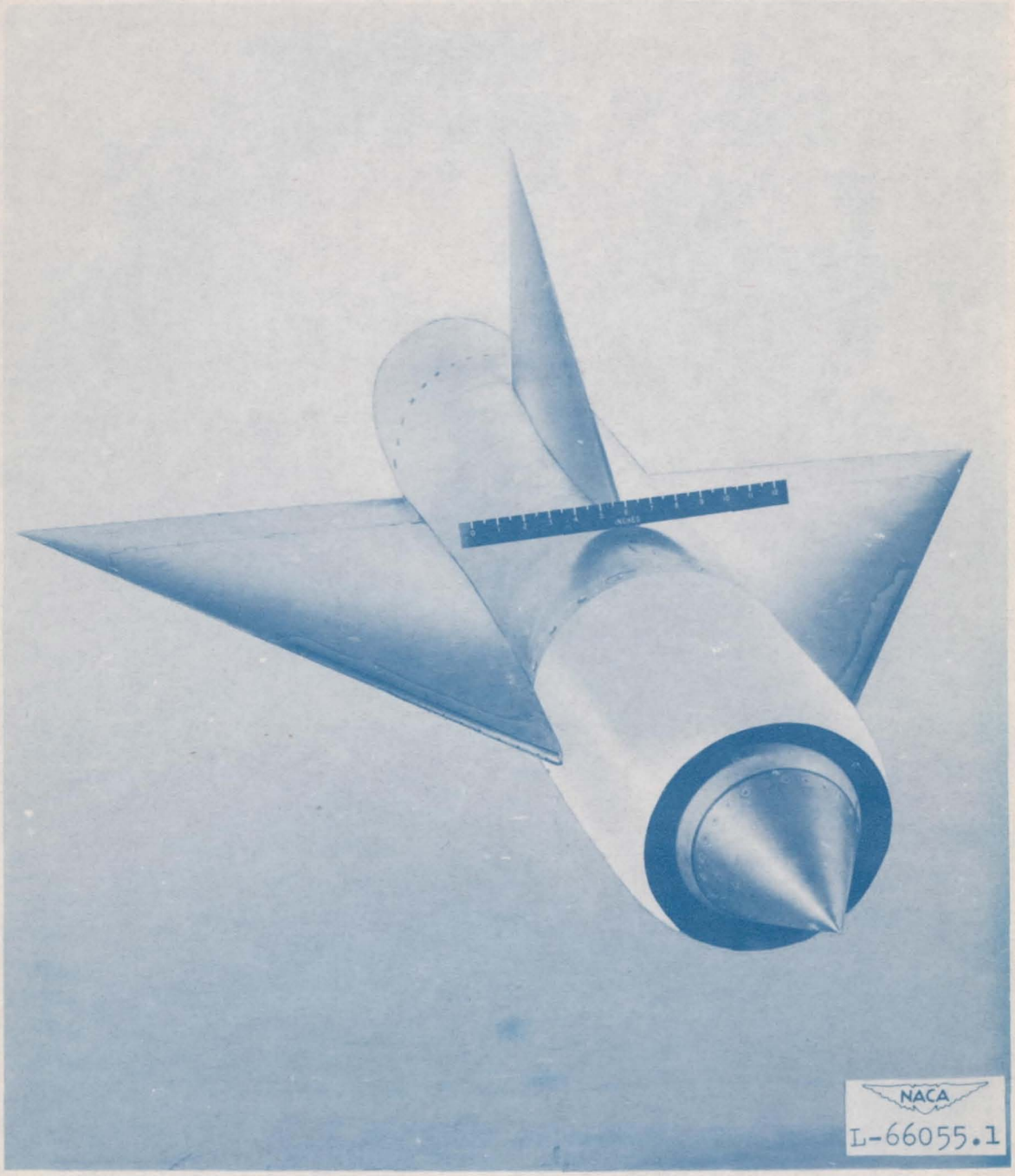

Figure 5.- Three-quarter view of model.

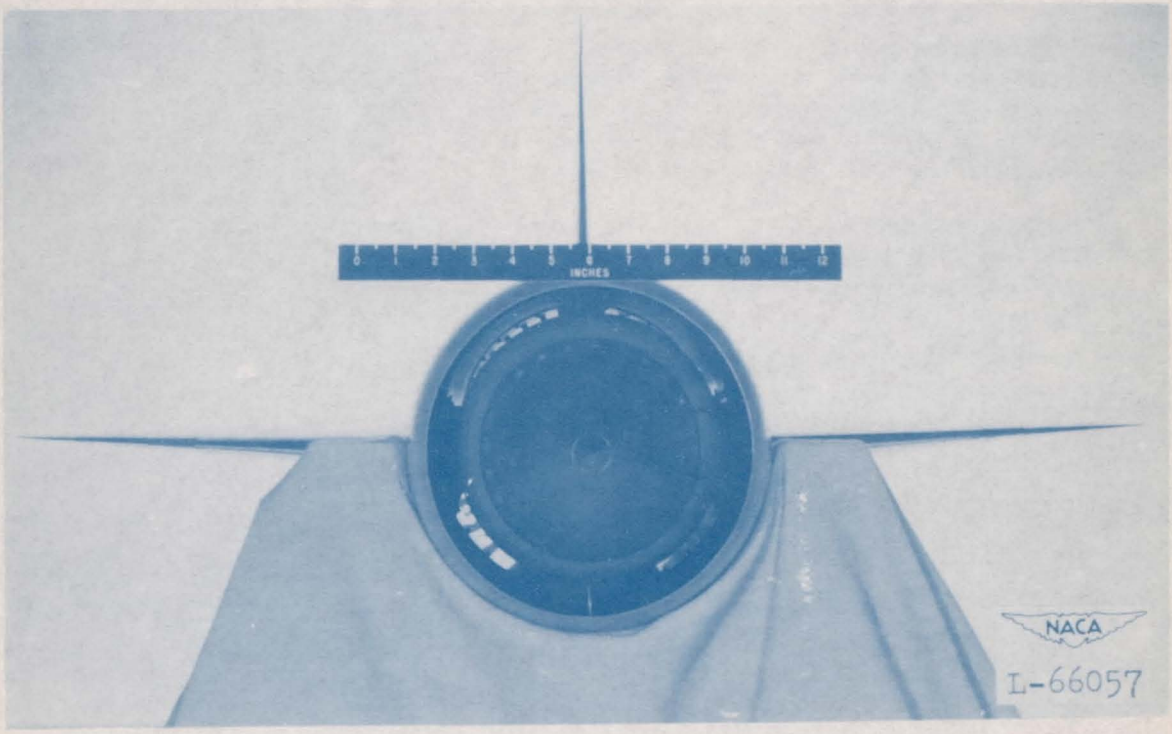

Figure 6.- Front view of model.

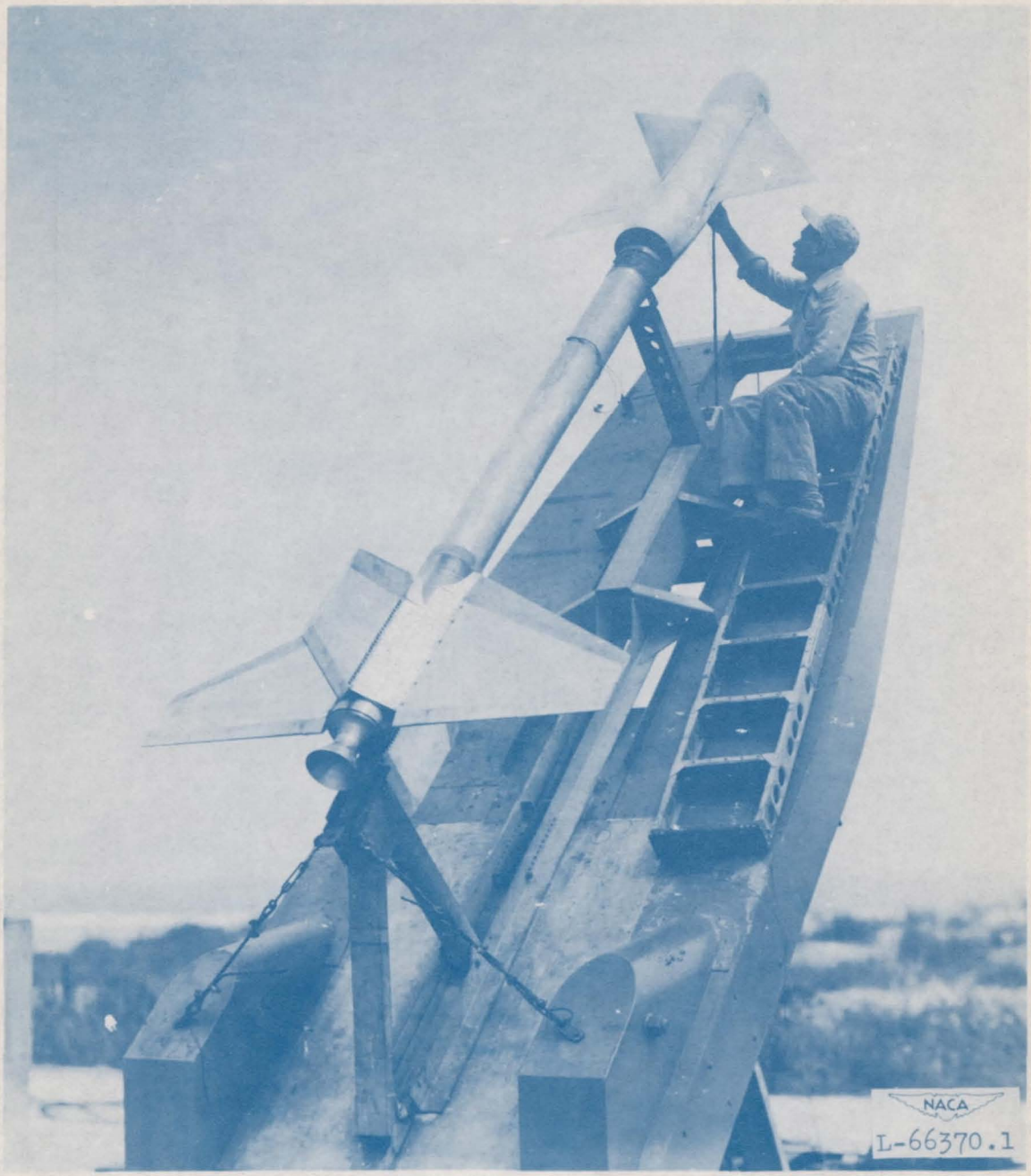

Figure 7.- Model-booster combination on launcher.

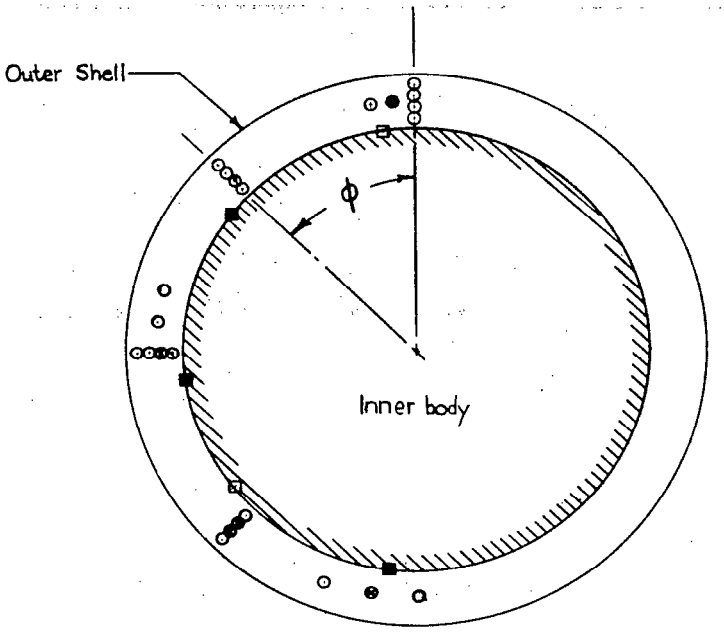

Location of Survey Points, Station 47

○ Ground-Test Total-Pressure Orifice
× Flight - Test Total-Pressure Orifice
□ Ground - Test Wall Static Orifice
✱ Flight - Test Wall Static Orifice

NACA

Figure 8.- Plane of survey station, looking forward.

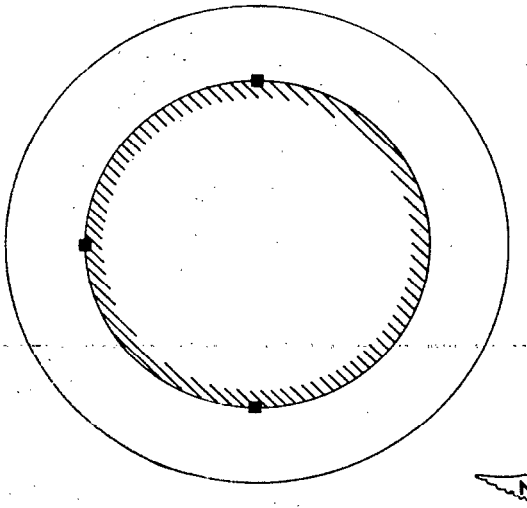

NACA

Location of Exit Statics, Station 57.83

Figure 9.- Location of exit survey, looking forward.

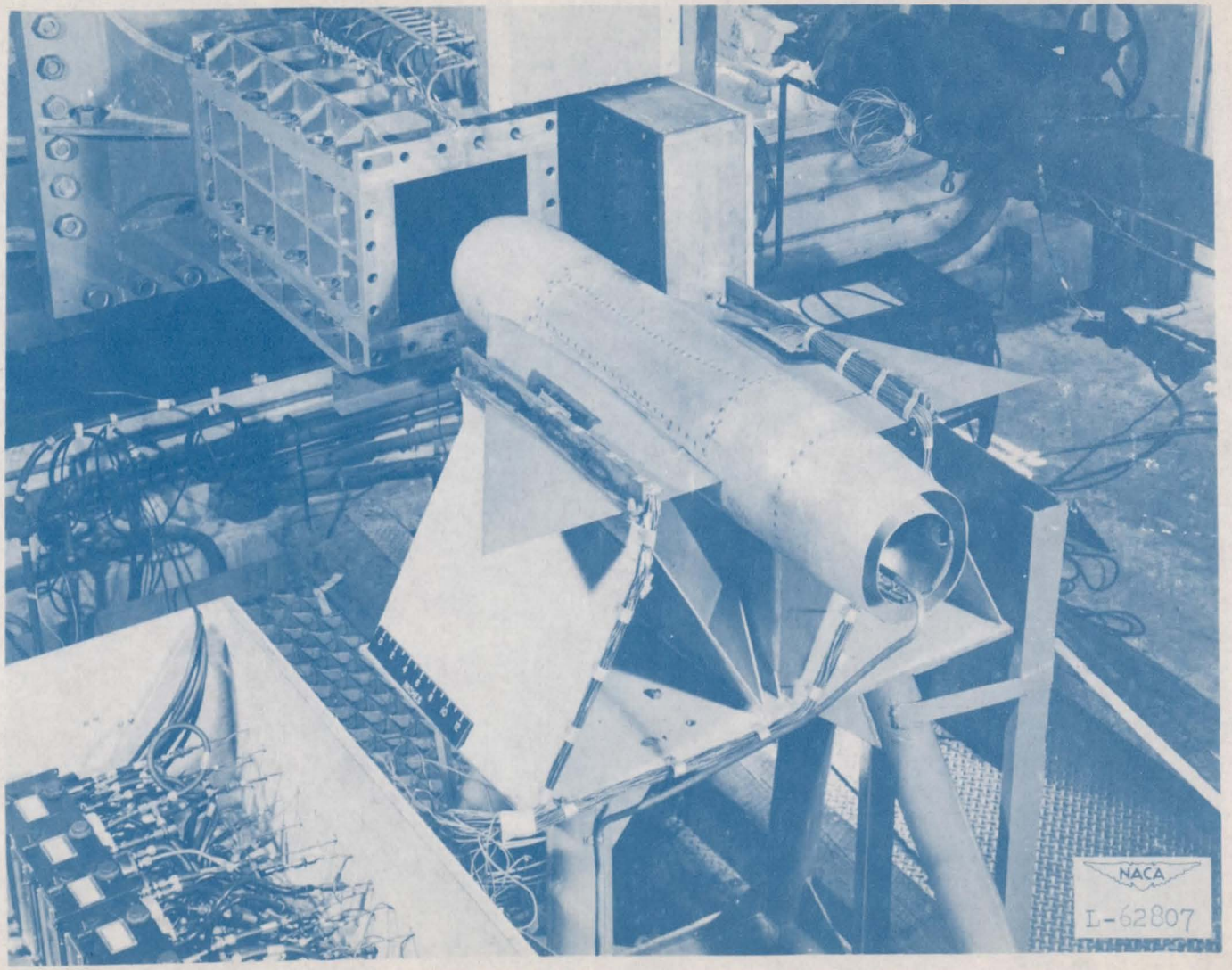

Figure 10.- Ground setup of model in the preflight free jet for test at M = 1.4.

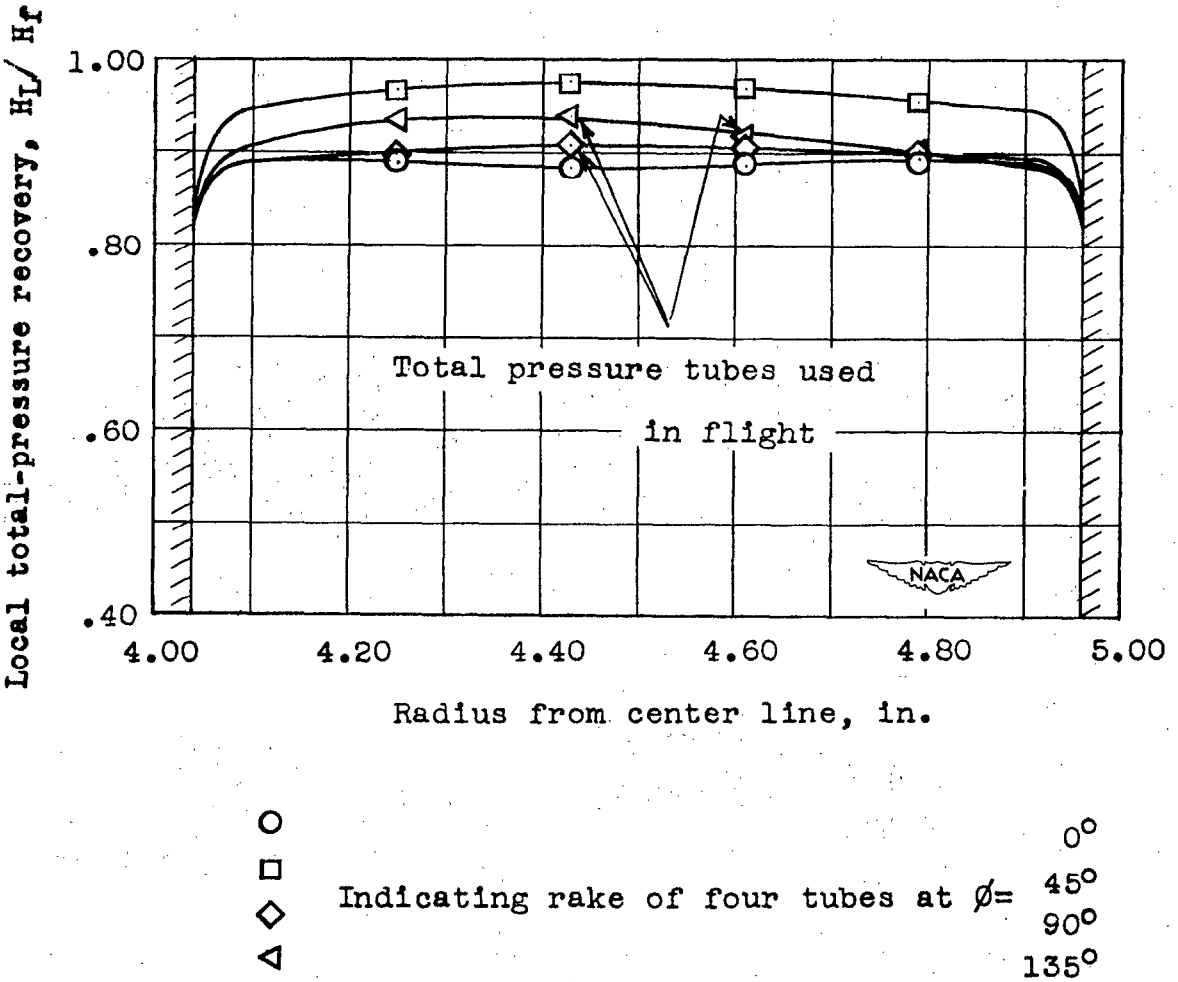

Figure 11.- Radial distribution of local total-pressure recovery at station 47, at M = 0.71, from the ground test.

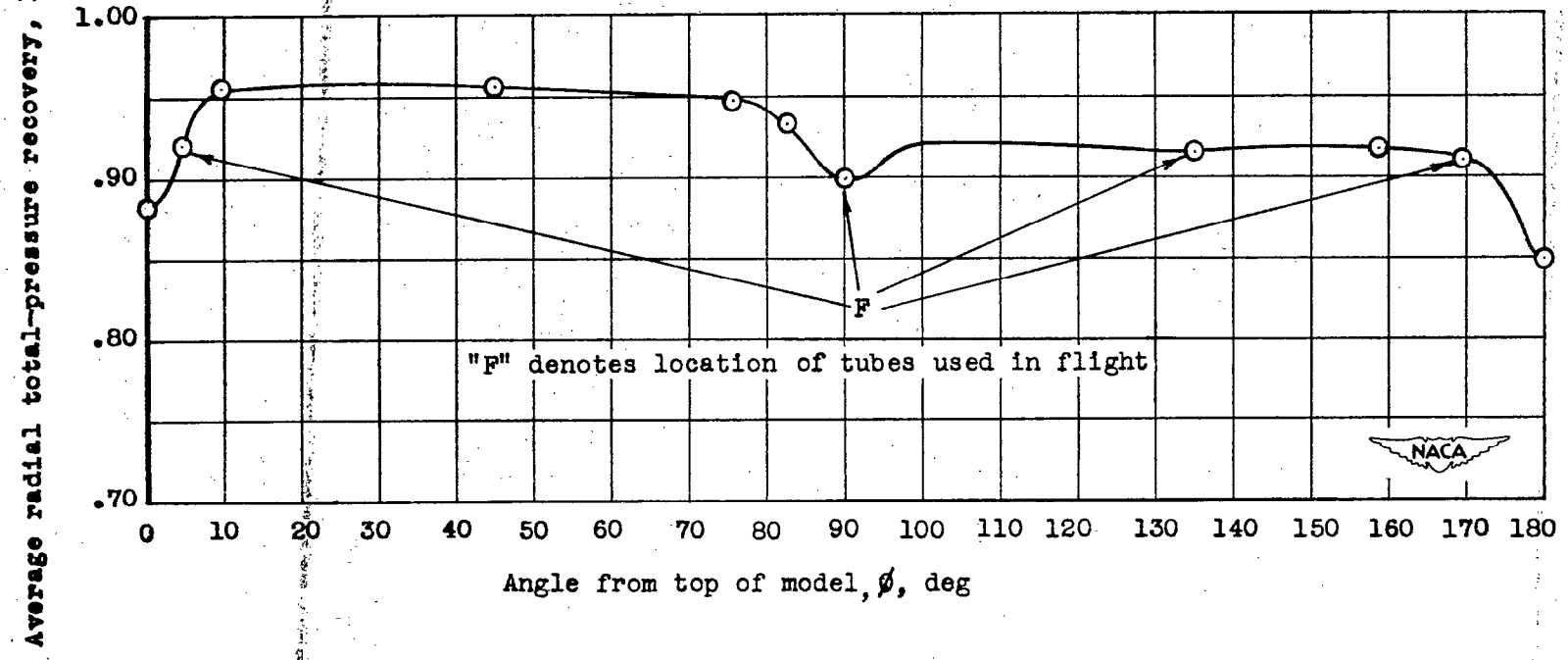

Figure 12.- Angular distribution of average radial total-pressure recovery at station 47, at M = 0.71, from the ground test.

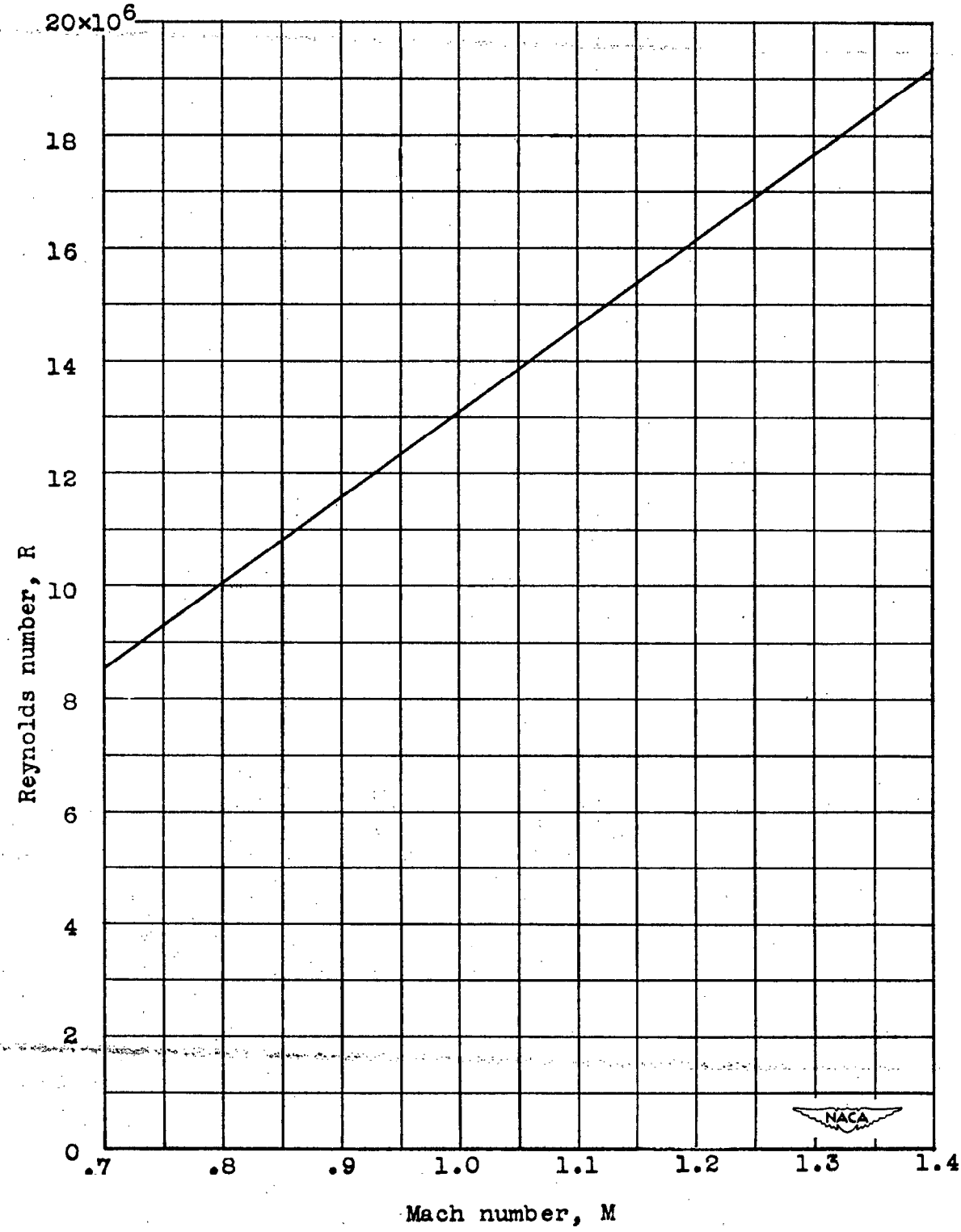

Figure 13.- Variation of Reynolds number with Mach number.

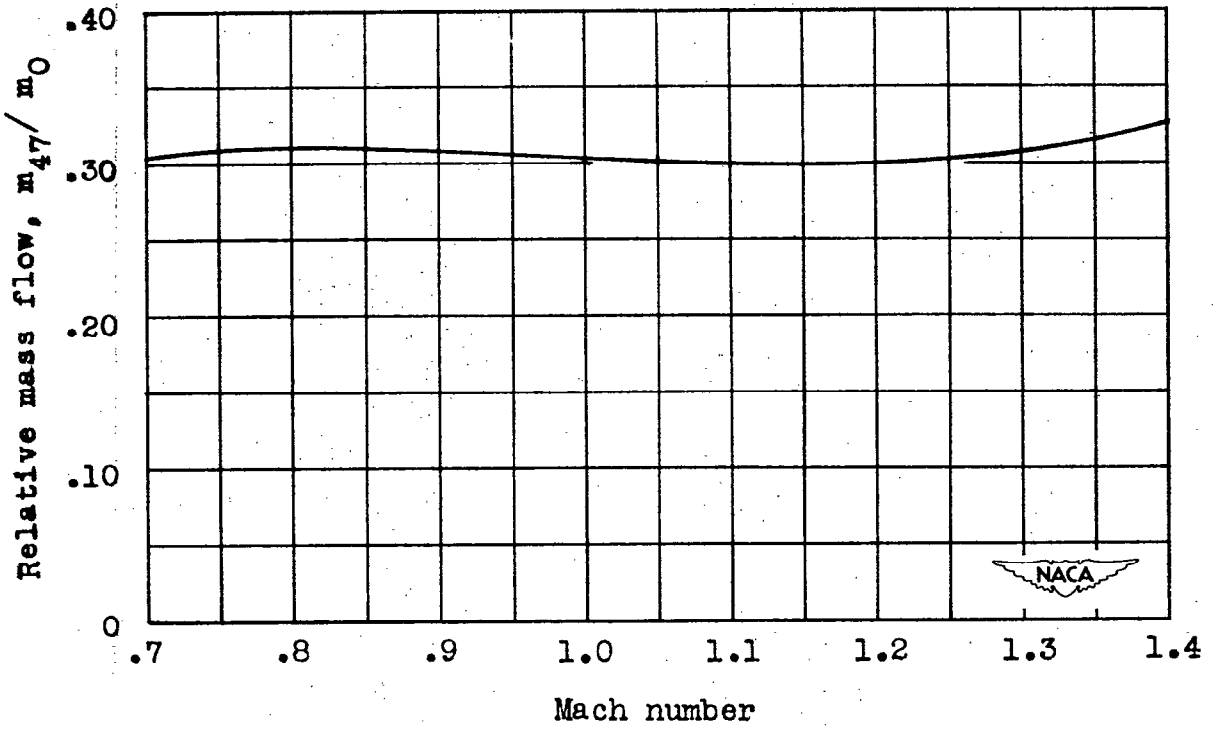

Figure 14.- Variation of relative mass flow with Mach number.

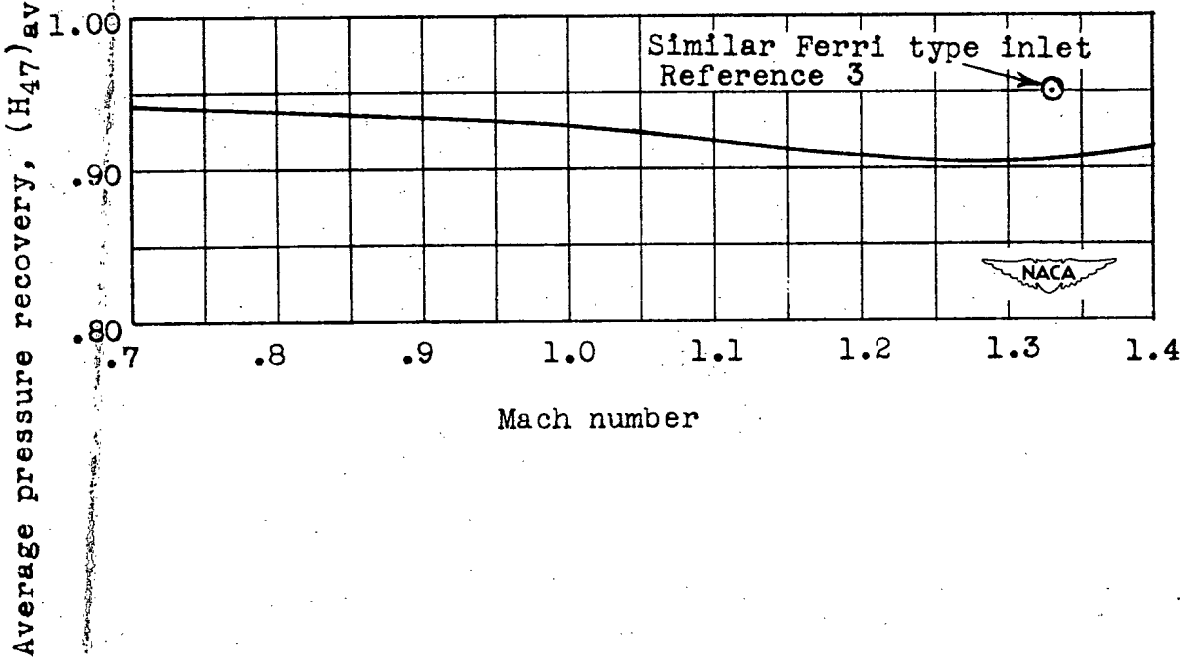

Figure 15.- Average total-pressure recovery at station 47; $M_{47_{av}} = 0.44$.

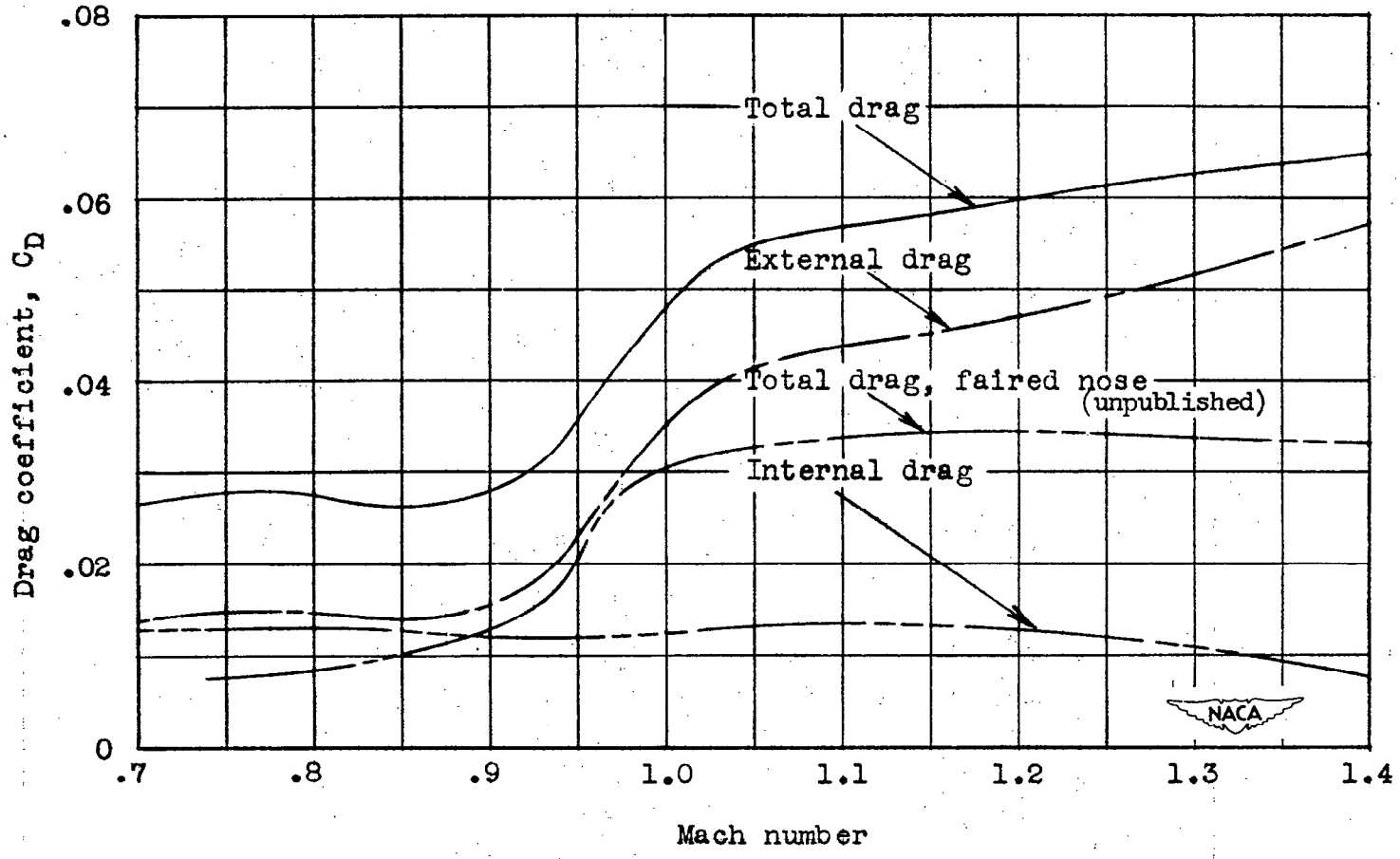

Figure 16.- Results of drag measurements and a comparison with the unpublished drag of the modified XF-92.